Hardness Prediction System for Multi-pass Weld Metal of Low-alloy Steel Using Neural Network

Lina YU*

* Corresponding author

Osaka University

2-1 Yamadaoka, Suita, Osaka, 565-0871, JAPAN

E-mail: yulina@mapse.osaka-u.ac.jp

Kazutoshi NISHIMOTO

Osaka University

2-1 Yamadaoka, Suita, Osaka, 565-0871, JAPAN

E-mail: nisimoto@mapse.osaka-u.ac.jp

Kazuyoshi SAIDA

Osaka University

2-1 Yamadaoka, Suita, Osaka, 565-0871, JAPAN

E-mail: saida@mapse.osaka-u.ac.jp

Hardness Prediction System for Multi-pass Weld Metal of Low-alloy Steel Using Neural Network

Lina Yu[1], Kazutoshi Nishimoto[1] and Kazuyoshi Saida[1]

[1] Graduate School of Engineering, Osaka University, Japan

Abstract: Multi-pass welds are subjected to various thermal cycles and have a complicated microstructure distribution; therefore, defects can easily occur. To prevent the defects, it is important to select the appropriate welding conditions before welding. Hardness is the most convenient criterion for the safety evaluation. A hardness prediction system for the heat-affected zone (HAZ) of a multi-pass weld has been proposed by the authors. However, in actual welding, defects can occur not only in the HAZ, but also in the weld metal (WM) of a multi-pass weld. Therefore, in this study, hardness prediction system for the WM of a multi-pass weld was developed based on a neural network and database of experimental measurements, a new hardness prediction system of WM has been developed by using neural network. In addition, a hardness prediction system for an entire multi-pass weld, including both the WM and HAZ, was developed by combining the new system with the previously proposed hardness prediction system for the HAZ. Therefore, the hardness values for both the WM and HAZ could be predicted based on the simulated thermal cycles of multi-pass welding, and the calculated values were found to be in good agreement with the measured results. This indicated that the newly developed hardness prediction system for multi-pass welds, including both the WM and HAZ, was effective for selecting appropriate welding conditions prior to actual multi-pass welding.

Keywords: Hardness prediction, Multi-pass welding, Weld metal, Neural network, Low-alloy steel

1. Introduction

Multi-pass welding is typically required when thick sections need to be welded. This technique is used in the industry to join thick sections, and perform repairs, build ups, surface hard-facing, etc. Multi-pass welding has many benefits; however, as the name suggests, multi-pass welds consist of multiple passes of welding in a joint. Thus, the microstructure of a multi-pass weld varies significantly from that of a single-pass or two-pass weld [1,2]. Multi-pass welds are subject to multiple thermal cycles and have a complicated microstructure distribution; therefore, defects can easily occur. To prevent defects, it is important to select the appropriate welding conditions before the actual multi-pass welding. For example, Caron et al. [3] investigated the effects of the welding heat input and weld bead depth-to-width ratio on the cracking susceptibility of a multi-pass weld. Abdullah et al. [4] discussed the effects of the number of welding passes and electrode type on the mechanical properties of a multi-pass weld. Mashhuriazar et al. [5] investigated the effects of pre-weld heat treatment and the heat input on the metallurgical and mechanical behaviors of the heat-affected zone (HAZ) of a

multi-pass weld. However, in theory, the metallurgical and mechanical properties of the weld are directly determined by the complicated multi-pass thermal cycles during multi-pass welding. Therefore, the variables investigated in this study were the parameters of the thermal cycles that occur during the multi-pass welding.

Hardness is one of the key criteria for evaluating the mechanical behavior of a multi-pass weld, and hardness is the most convenient criterion for the safety evaluation [4,5]. A prediction system for the hardness of the HAZ of a multi-pass weld was previously proposed by the authors [6-8]. However, during actual multi-pass welding, defects can occur not only in the HAZ but also in the weld metal (WM) of the multi-pass weld, such as cracking, porosity, lack of fusion [9-11]. Therefore, in order to select the appropriate welding conditions before the actual multi-pass welding, a prediction system for the hardness of the WM of a multi-pass weld was developed using a neural network in this study.

The hardness values of the WM and HAZ are determined by various factors such as the peak temperature (T_p) and cooling rate (CR) of the welding thermal cycles. Therefore, a new hardness prediction system for the WM of a multi-pass weld was developed using a neural network, which can process the complex data involved. Furthermore, a hardness prediction system for an entire multi-pass weld, including both the WM and HAZ, was developed by combining the new system with the previously proposed hardness prediction system for the HAZ [6-8]. Using this, the hardness values of both the WM and HAZ could be predicted based on the simulated thermal cycles during multi-pass welding. In addition, the newly developed hardness prediction system for the entire multi-pass welds was validated by comparing the predicted hardness values for both the WM and HAZ after multi-pass welding with the measured results. Therefore, appropriate welding parameters can be selected prior to actual multi-pass welding.

2. Methodology

2.1 Materials

In this study, the low-alloy steel A533B was used as the base material, and MG-S56X with a wire diameter of ⌀1.2 mm was used as the filler material for multi-pass welding. The MG-S56X and A533B steel have similar compositions, and their chemical compositions are listed in Table I.

Table I Chemical compositions of the materials used in this study

Material	Chemical compositions (mass %)												
	C	Si	Mn	P	S	Ni	Cu	Cr	Mo	Ti	Al	Fe	Co
A533B (Base metal)	0.12	0.26	1.43	0.006	0.002	0.53	0.02	0.01	0.51	0.001	0.04	Bal.	-
MG-S56X (Filler metal)	0.06	0.43	1.51	0.006	0.005	0.89	0.03	0.04	0.35	0.09	0.01	Bal.	<0.01

2.2 Preparation of the raw WM

The raw WM part (MG-S56X) was the WM after only one welding pass. To prepare the raw WM

sample with a larger size, five welding passes were performed as shown in Fig. 1(a), and then the raw WM sample with a size of 10×5×2.5mm was cut from the 5th pass (the last pass) weld metal, as schematically illustrated in Fig. 1(b). Five tungsten inert gas (TIG) welding passes were performed on the specimen illustrated in Fig. 2, under the welding conditions listed in Table II.

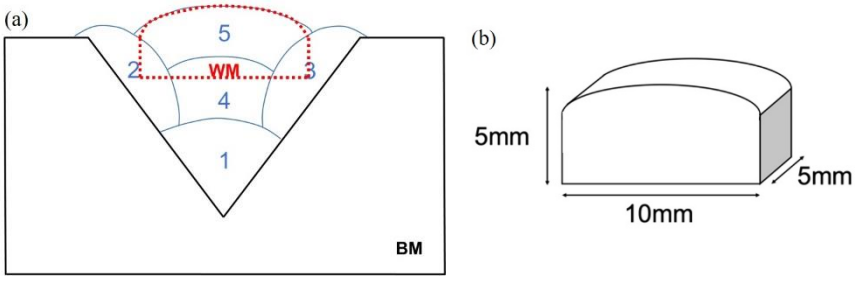

Fig. 1 Preparation method of the raw WM part:
(a) sample cut from the 5-pass weld, and (b) specimen size of the raw WM sample.

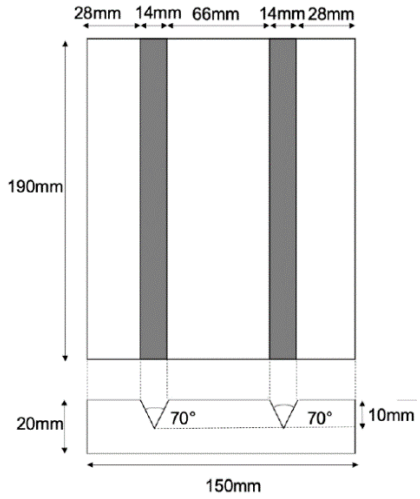

Fig. 2 Specimen for multi-pass welding.

Table II Welding conditions for TIG welding

Current (A)	Voltage (V)	Wire sending speed (mm/s)	Welding speed (mm/s)	Heat input (kJ/mm)
250	15.3	50	1.67	2.29

2.3 Simulated thermal cycles on the raw WM

The simulated thermal cycles on the raw WM (MG-S56X) were produced using a high-frequency induction heating device, and the thermal history of the heating and cooling processes was obtained using a thermocouple. As shown in Fig. 3, four types of thermal cycles were used in this study, which

could simulate the typical thermal cycles that may be generated during multi-pass welding [8,12]. More complicated thermal cycles could also be simplified as four typical thermal cycles through the simplification method proposed by the authors [7]. The Ac_1 and Ac_3 transformation temperatures of A533B/MG-S56X were 670 °C and 837 °C, respectively. The parameters of the four typical thermal cycles are listed in Table III. It should be noted that the thermal cycle parameters were set directly by the high-frequency induction heating device. The peak temperature (T_p) of the thermal cycles ranged from 400 °C to 1350 °C, with the cooling rate (CR) varying from 10 °C/s to water quenching (WQ, CR ≈ 2000°C/s). It should be noted that T_{pi} is the T_p value of the i^{th} pass cycle, and CR_i is the CR between 800 °C and 500 °C during the i^{th} pass cycle. For the tempering cycle, the temper temperature was lower than Ac_1. Thus, the temper temperature (T_{te}) was changed from 400 °C to 650 °C, while varying the holding time (t_{te}) from 5 s to 5400 s.

After polishing and etching with a 3% nital solution, the Vickers hardness was measured under a load of 9.8 N for 20 s, and the average value, excluding the maximum and minimum values, was taken from multiple measurements in this study. Scanning electron microscopy (SEM) was used to observe the microstructures.

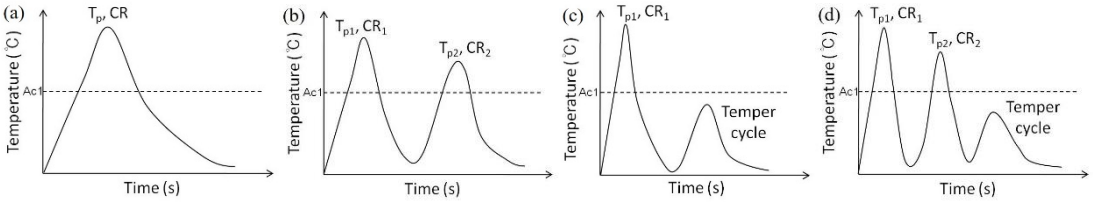

Fig. 3 Four kinds of simulated thermal cycles that could be generated in the WM during multi-pass welding:

(a) 1-cycle, (b) 2-cycle, (c) 1-cycle+tempering, and (d) 2-cycle+tempering.

Table III Parameter variation ranges for four kinds of thermal cycles

Parameters	T_{p1} (℃)	CR_1 (℃/s)	T_{p2} (℃)	CR_2 (℃/s)	T_{te} (℃)	t_{te} (s)
1-cycle	400-1350	10, 60, WQ				
2-cycle	700-1350	10, 60, WQ	700-1200	10, 60, WQ		
1-cycle +tempering	1350	10, 60, WQ			400-650	5-5400
2-cycle +tempering	1350	10, 60, WQ	700-1200	10, 60, WQ	400-650	5-5400

2.4 Multi-pass welding process procedure

To verify the effectiveness of the developed hardness prediction system for the WM of a multi-pass weld, a 19-pass welding test was performed on the A533B steel base metal using the MG-S56X wire,

as illustrated in Fig. 4, under the same welding conditions listed in Table II. After the 19-pass welding, the hardness values of both the WM and HAZ were measured at the section surface.

The thermal cycles during multi-pass welding were simulated using the thermal elastic plastic finite element method (FEM) software JWRIAN, which was specifically developed for predicting the thermal history, residual stress, and deformation of a weld [13]. The temperature dependences of the physical properties of A533B/MG-S56X [14] are presented in Table IV.

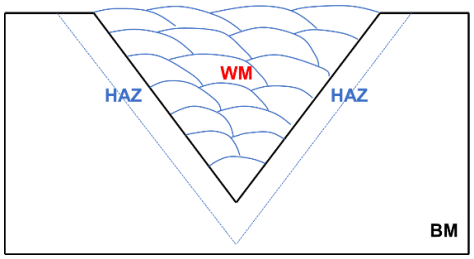

Fig. 4 Schematic illustration of the 19-pass weld.

Table IV Temperature dependences of physical properties of A533B/MG-S56X steel

Temperature (°C)	Specific heat (J/kg°C)	Thermal conductivity (W/mm°C)	Yield Strength (MPa)	Young's modulus (GPa)	Poisson's ratio (-)	Thermal expansion (1/°C)
20	445	0.039	478	210	0.3	12.0e-6
200	517	0.0389	455	202	0.3	12.7e-6
400	592	0.036	405	188	0.3	13.9e-6
600	723	0.0317	238	160	0.3	13.8e-6
800	812	0.0378	75	115	0.3	12.6e-6
1000	658	0.0309	17	93	0.3	12.6e-6
1300	721	0.0365	5	10	0.3	14.5e-6

3. Experimentally measured hardness database of WM

The hardness values of the raw WM (MG-S56X) samples subjected to the simulated thermal cycles listed in Table III were measured experimentally, and could be used as a hardness database for the WM hardness prediction system. The hardness database and microstructures after the four types of thermal cycles are discussed in the following.

3.1 Hardness database of MG-S56X after 1-cycle

Fig. 5 presents the relationship between the average hardness of the raw WM (MG-S56X) subjected to 1-cycle and T_{p1}, with CR_1 varying from 10 °C/s to WQ (2000 °C/s), with the error bar shown in the figure. At the high CR_1 of WQ, the hardness increased significantly with T_{p1}. However, when CR_1 was lower than 60 °C/s, the hardness did not increase monotonically, and the peak hardness occurred at

approximately 700 °C, which was just slightly higher than the A_{c1} temperature of the low-alloy steel (A533B/MG-S56X).

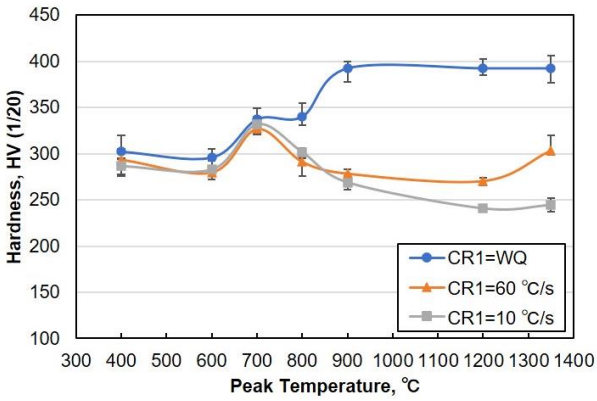

Fig. 5 Relationship between hardness of MG-S56X and T_{p1} after 1-cycle.

The microstructures of the as-received raw WM (MG-S56X) and WM samples subjected to the simulated 1-cycle at various peak temperatures with the high CR_1 of WQ are illustrated in Fig. 6. The microstructures of the WM samples subjected to the simulated 1-cycle at various T_{p1} values, with a low CR_1 of 10 °C/s, are presented in Fig. 7. The different microstructures may explain the different hardness changes that occurred at different cooling rates.

As shown in Fig. 6(a), the microstructure of the as-received raw WM was mainly bainite. After 1-cycle, as presented in Figs. 6-7, regardless of the cooling conditions, there was no significant change in the microstructure when T_{p1} was 600°C, which was lower than the A_{c1} point. When T_{p1} was changed to 700 °C and 800 °C, which was between A_{c1} and A_{c3}, phase transformation occurred in the WQ-cooled sample, resulting in a mixed structure consisting of martensite-austenite (M-A) and the remaining bainite. When T_{p1} was increased to 900 °C and 1350 °C, which were higher than A_{c3}, lath martensite could be observed in the WQ-cooled sample, which explained the high hardness. In contrast, after cooled with a low CR_1 of 10 °C/s, the sample contained a mixed microstructure of ferrite and residual bainite with T_{p1} changed to 700 °C. When T_{p1} exceeded 800 °C, mainly granular bainite and ferrite were found in the sample with a low CR_1 of 10 °C/s, which may be the reason for the low hardness. Therefore, the hardness changes were significantly different with different cooling rates.

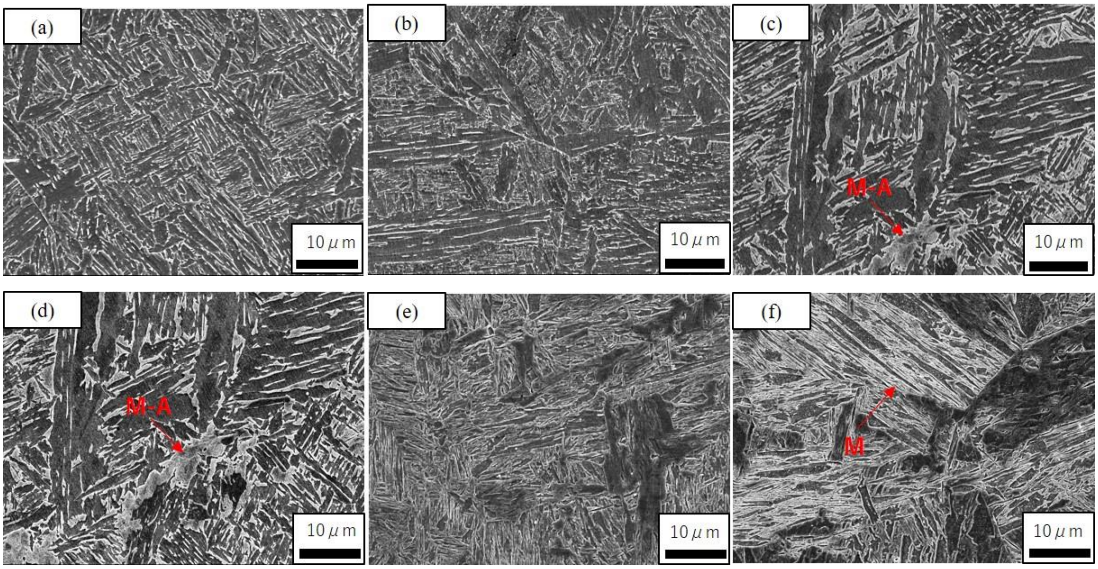

Fig. 6 Microstructures of MG-S56X after 1-cycle with CR_1 = WQ:
(a) as-received raw WM, (b) T_{p1} = 600 ℃, (c) T_{p1} = 700 ℃, (d) T_{p1} = 800 ℃, (e) T_{p1} = 900 ℃, and (f) T_{p1} = 1350 ℃.

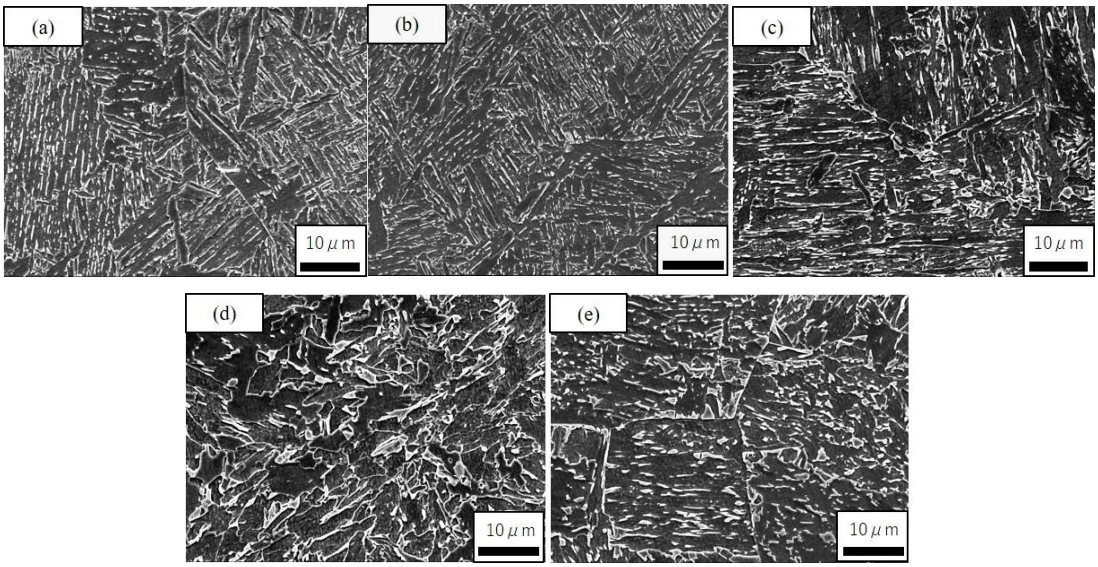

Fig. 7 Microstructures of MG-S56X after 1-cycle with CR_1 = 10 ℃/s:
(a) T_{p1} = 600 ℃, (b) T_{p1} = 700 ℃, (c) T_{p1} = 800 ℃, (d) T_{p1} = 900 ℃, and (e) T_{p1} = 1350 ℃.

3.2 Hardness database of MG-S56X after 1-cycle+temperinging

The tempering effects of multiple passes of the tempering cycles with T_{te} varying from 400 °C to 650 °C, could be characterized by a newly proposed thermal cycle tempering parameter (TCTP), which was previously proposed by the authors [6]. The TCTP can extend the application of Larson-Miller parameter from isothermal to non-isothermal heat treatment, and the proposed TCTP has been

proved to be applicable for quantitatively evaluating the tempering effect and hardness change during both thermal cycle tempering processes and multi-pass isothermal heat treatment.

Fig. 8 illustrates the relationship between the hardness of the WM (MG-S56X) and the TCTP after 1-cycle+tempering at different T_{p1} values. For all T_{p1} conditions, the hardness after the tempering cycle first decreased with an increase in the TCTP, reaching a minimum value when the TCTP was approximately 15000. Subsequently, the hardness increased with the TCTP and reached a maximum value when TCTP was approximately 17000. Finally, the hardness decreased with a further increase in the TCTP. This indicated that secondary hardening occurred after the tempering cycle in the WM of MG-S56X. The hardness change tendency was more remarkable for samples subjected to a higher T_{p1} of 1350 °C and faster CR_1 of WQ because the hardness change range was larger than that with a lower T_{p1} and slower CR_1.

The SEM observed microstructures of the WM (MG-S56X) after 1-cycle+tempering at different TCTP values are presented in Fig. 9, when the 1st cycle was fixed at T_{p1} = 1350 °C and CR_1 = WQ. As shown in Fig. 6(f), lath martensite was observed in the matrix before tempering. After different tempering cycles with different TCTP values, as illustrated in Fig. 9, inter-lath precipitates were observed in the martensite structure under all conditions; however, there was little difference in size.

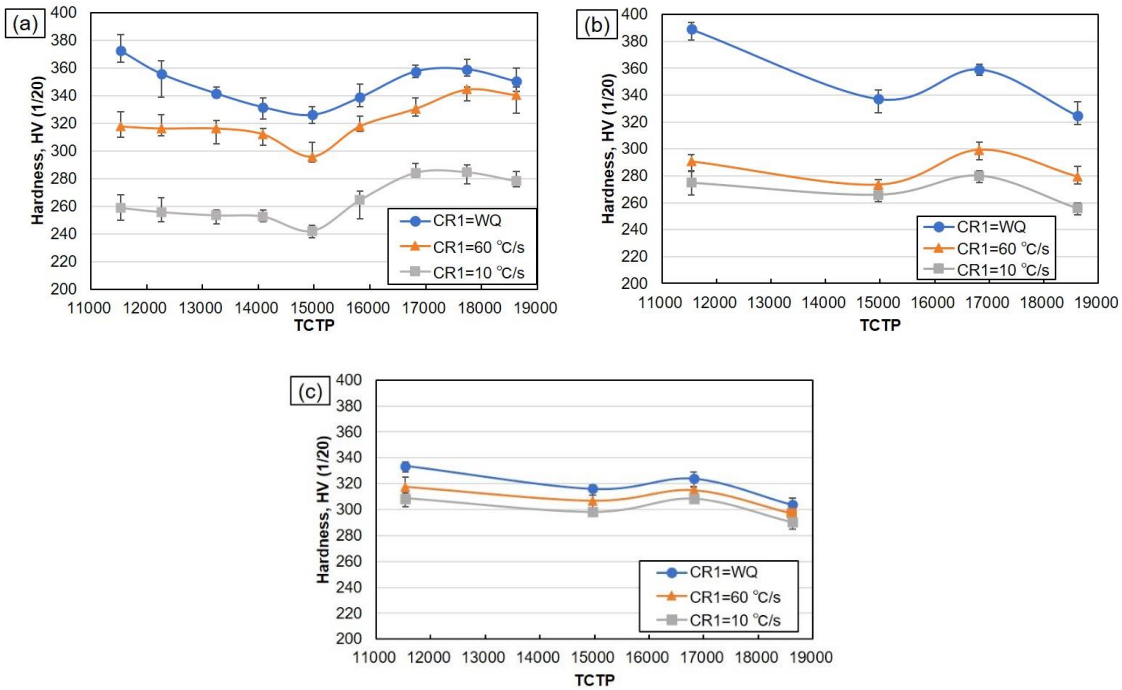

Fig. 8 Relationship between hardness of MG-S56X and TCTP after 1-cycle+tempering: (a) T_{p1} = 1350 ℃, (b) T_{p1} = 900 ℃, and (c) T_{p1} = 800 ℃.

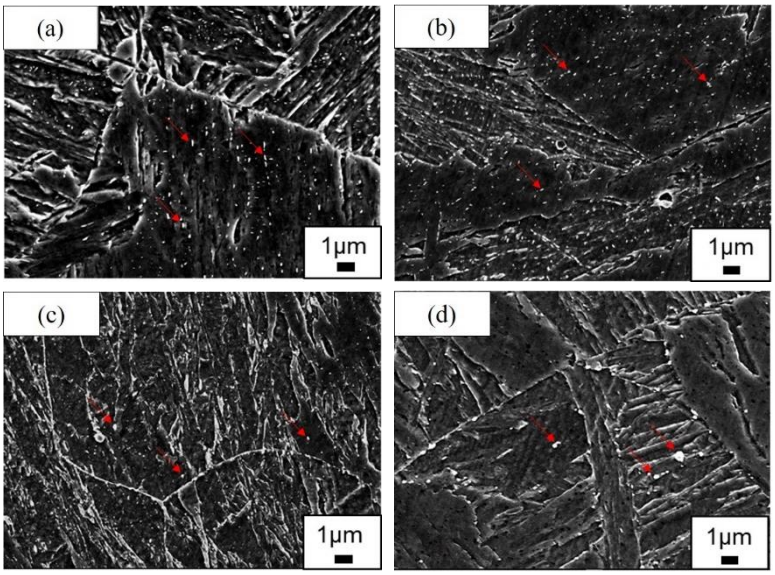

Fig. 9 Microstructures of MG-S56X after 1-cycle+tempering (T_{p1} = 1350 ℃, CR_1 = WQ): (a) T_{te} = 400 ℃, t_h = 5 s (TCTP = 11537), (b) T_{te} = 600 ℃, t_h = 5 s (TCTP = 15823), (c) T_{te} = 650 ℃, t_h = 600 s (TCTP = 17742), (d) T_{te} = 650 ℃, t_h = 5400 s (TCTP = 18623).

The secondary hardening that occurs in the WM (MG-S56X) after a tempering cycle can generally be attributed to the following three events: (1) the precipitation of Mo-carbide, (2) MnS precipitation and (3) the precipitation of TiC.

Concerning the Mo-carbide precipitation, according to previous studies [15-17], Mo has been found to only delay softening, and no secondary hardening has been observed when the Mo content was less than 1 mass%. However, when the Mo content was more than 2 mass%, secondary hardening could occur owing to the precipitation of Mo_2C. The Mo contents in the raw WM (MG-S56X) and BM (A533B) in this study were 0.35 and 0.51 mass% respectively, which are much lower than 2 mass%. In addition, no secondary hardening was observed in the BM of A533B, and the hardness decreased linearly with an increase in the TCTP after the tempering cycle [8]. This proved that Mo_2C precipitation was not the reason for the secondary hardening in the WM (MG-S56X).

In relation to the second possible reason for MnS precipitation, it's well known that there are two types of MnS in steel: a non-solid solution type of MnS, which precipitates only by quenching from high temperatures over 1400 ℃ during solidification and does not precipitate in the temper temperature range; and a solid solution type of MnS, which precipitates only when T_p is between 1200 ℃ and 1000 ℃ with an ultra-low CR of less than 1 ℃/s [18,19]. Therefore, these two types of MnS were not considered to be the reason for the secondary hardening during the tempering cycle with a T_p lower than 650 ℃ in the WM (MG-S56X).

In addition to the precipitation of Mo-carbide and MnS, the precipitation of TiC is considered to be the most probable reason for the occurrence of secondary hardening during a tempering cycle because

Ti is reported to easily cause secondary hardening when even a small amount is added [20,21]. The hardness change in 0.1Ti steel after a tempering cycle was similar to the result for the WM of MG-S56X. The same amount of Ti was present in the raw WM of MG-S56X as in 0.1Ti steel. Therefore, the secondary hardening in the two types of steel was considered to have the same cause. Based on a three-dimensional atom probe analysis, no TiC could be confirmed when the TCTP was approximately 14000, but TiC was clearly observed when the TCTP was approximately 17000 [21]. This suggested that the precipitation of TiC was the most probable reason for the secondary hardening during the tempering cycle of the WM, owing to the addition of Ti to the MG-S56X filler metal.

3.3 Hardness database of MG-S56X after 2-cycle and 2-cycle+tempering

In order to simulate the 2-cycle and 2-cycle+tempering conditions that could have been generated in the WM after multi-pass welding, many specimens were tested, and the hardness was determined using four and five parameters respectively. Figs. 10 and 11 illustrate some examples of the measured hardness results for the WM (MG-S56X) after 2-cycle and 2-cycle+tempering, respectively.

Fig. 10 presents the relationships between the hardness of the WM (MG-S56X) after 2-cycle and T_{p2} for different CR_2 values for the 2nd cycle, with the 1st cycle fixed. When CR_2 was changed from 10 °C/s to WQ, different hardness change tendencies were observed, which were similar to the results for 1-cycle.

The relationships between the hardness of the WM (MG-S56X) after 2-cycle+tempering and the TCTP with different CR_2 values are illustrated in Fig. 11, with the other three parameters being constant. Secondary hardening was also observed after the 2-cycle+tempering, which may have been caused by the precipitation of TiC during the tempering cycle.

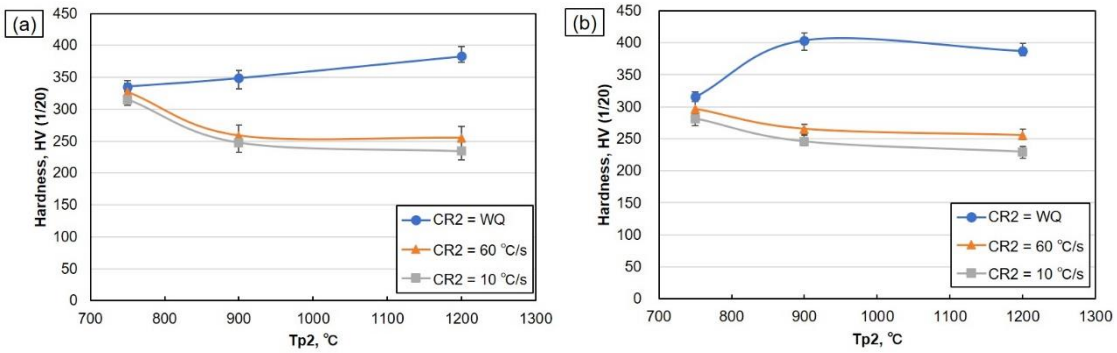

Fig. 10 Relationships between hardness of MG-S56X and T_{p2} for different CR_2 values after 2-cycle: (a) T_{p1} = 1350 ℃, CR_1 = WQ, and (b) T_{p1} = 1350 ℃, CR_1 = 30 ℃/s.

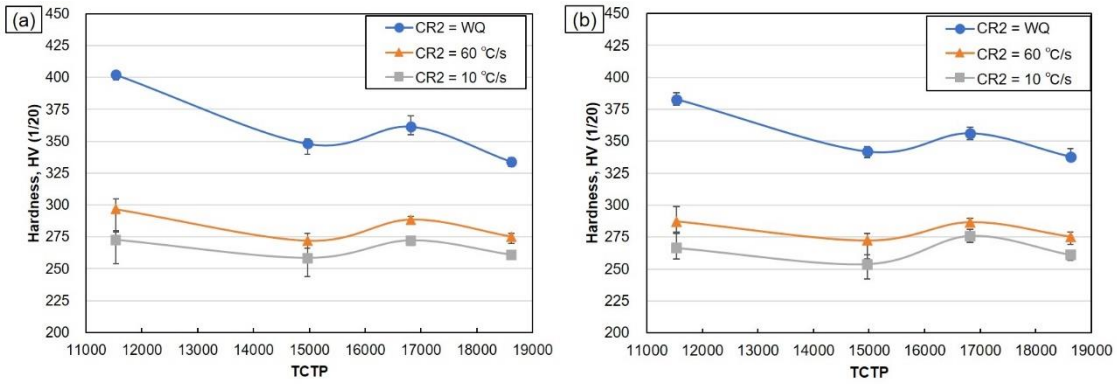

Fig. 11 Relationships between hardness of MG-S56X and TCTP for different CR_2 values after 2-cycle+tempering:

(a) T_{p1} = 1350 ℃, CR_1 = WQ, T_{p2} = 900 ℃, and (b) T_{p1} = 1350 ℃, CR_1 = 60 ℃/s, T_{p2} = 900 ℃.

4. Neural network-based hardness prediction subsystem for WM

Based on the experimentally measured hardness database shown in section 3, a hardness prediction subsystem for the WM in multi-pass welding was developed by using a neural network (NN) [22,23], which is a useful modeling tool for nonlinear statistical data and commonly used to process complex relationships between inputs and outputs or to find patterns in data.

4.1 FBF-NN

The radial basis function (RBF) [24] is a powerful technique for interpolating a multidimensional space in an NN. Fig. 12 illustrates the RBF-NN model, which usually includes three layers: an input layer, a hidden layer with a non-linear RBF activation function, and a linear output layer. The hidden layer can be described using a Gaussian basis function:

$$h(x) = \exp\{-(x-c)^2/r^2\} \quad (1)$$

where x is the input data, c is the center vector, and r is the Euclidean distance. In its basic form, all the inputs are connected to each hidden neuron.

The output, $O(x_i)$, of the network is thus obtained as follows:

$$O(x_i) = \sum_{j=1}^{n} w_j\, h_j(x_i) = \sum_{j=1}^{n} w_j \exp\{-(x_i - c_j)^2/r^2\} \quad (2)$$

where *n* is the number of neurons in the hidden layer, c_j is the center vector for neuron j, and w_j is the weight of the linear output neuron. The weights w_j, c_j, and r are determined in a manner that optimizes the fit between $O(x_i)$ and the data.

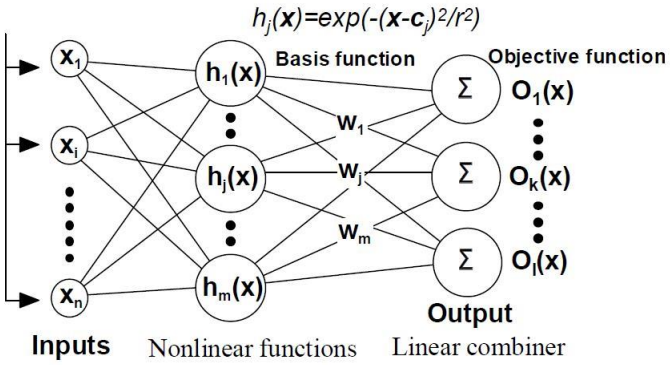

Fig. 12 RBF-NN model.

4.2 Prediction subsystem for hardness in WM

In this study, a prediction subsystem for the hardness in the WM of a multi-pass weld was developed, in which the thermal cycle parameters (T_{pi}, CR_i, and TCTP) were used as the input data, and the hardness of the WM (MG-S56X) was the output data. Table III lists the variation ranges of the input parameters in the proposed NN-based prediction subsystem. The thermal cycle parameters and experimentally measured hardness results for the WM (MG-S56X) were fed into the RBF-NN, and then the constants of w_i, c_i, and r were determined. Thus, the hardness prediction subsystem for the WM was developed by using the determined constants. It should be noted that previous research found that the hardness of low-alloy steel at a high CR of 100 °C/s was nearly equal to that cooled by WQ because the percentage of martensite remained constant with a CR higher than 100 °C/s [8], and the hardness of the WM (MG-S56X) mainly changed when the CR was lower than 60 °C/s. Therefore, the hardness prediction subsystem for WM developed in this study mainly focused on the CR range of 10-100 °C/s.

The results of the developed hardness prediction subsystem for WM (MG-S56X) subjected to the four types of thermal cycles are illustrated in Figs. 13-16. The relationship between the hardness of the WM (MG-S56X) and T_{p1}/CR_1 after 1-cycle is visually illustrated in the 3D and 2D contour figures of Figs. 13(a) and (b), respectively. The hardness is shown in different colors based on the different levels in the 2D contour figure. Thus, the hardness of the raw WM (MG-S56X) subjected to 1-cycle could be predicted when T_{p1} and CR_1 are known.

Figs. 14-16 show examples of the proposed hardness prediction subsystem results for the WM (MG-S56X) after 2-cycle, 1-cycle+tempering and 2-cycle+tempering, respectively. There were more than 2 input parameters in these subsystems. Therefore, the relationship between the WM hardness and only two input parameters could be visually illustrated when the other input parameters were fixed. For example, Fig. 14 shows the complex relationship between the hardness of the WM and T_{p2}/CR_2 of the 2nd cycle, with constant T_{p1} and CR_1 values of 1350 °C and 90 °C/s for the 1st cycle, respectively.

The four types of NN-based hardness prediction subsystems for the WM could be used to predict

the hardness of the raw WM (MG-S56X) exposed to any combination of thermal cycles if the thermal cycle parameters are known.

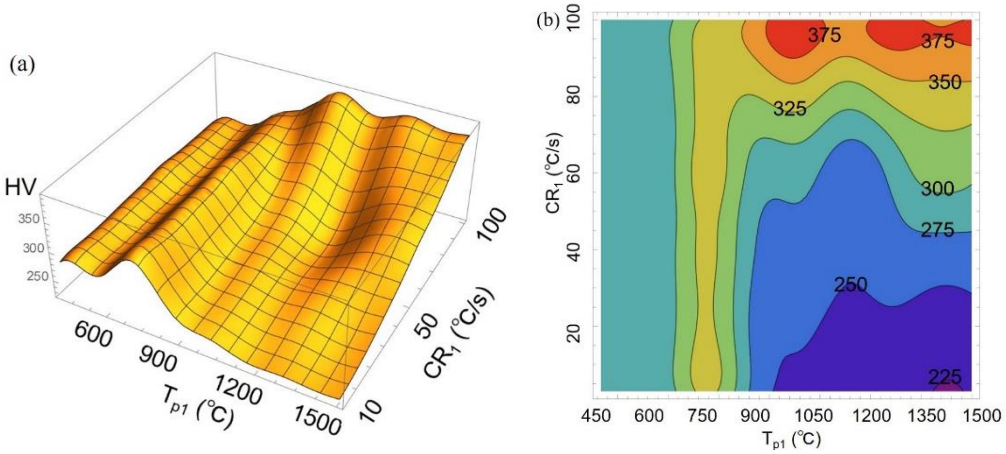

Fig. 13 Hardness prediction subsystem for WM after 1-cycle:
(a) 3D figure, and (b) 2D contour figure.

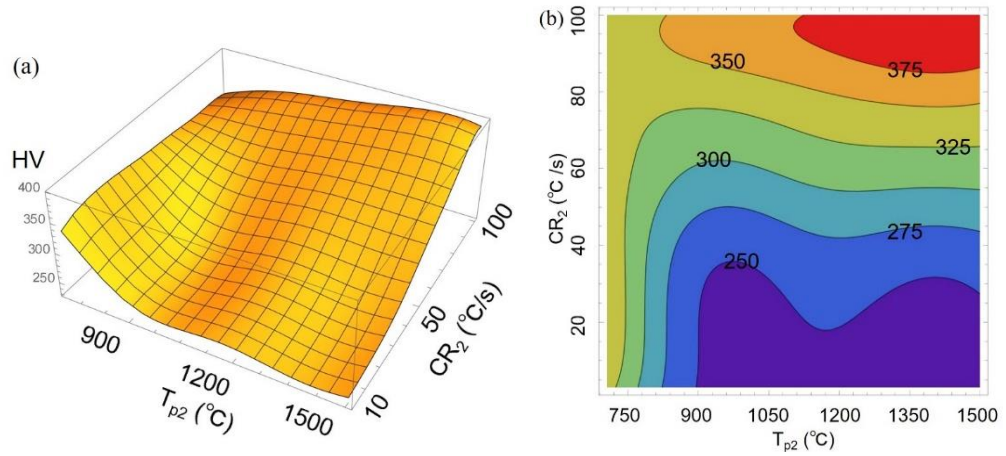

Fig. 14 Hardness prediction subsystem for WM after 2-cycle (with constant T_{p1} = 1350 °C, CR_1 = 90 °C/s):
(a) 3D figure, and (b) 2D contour figure.

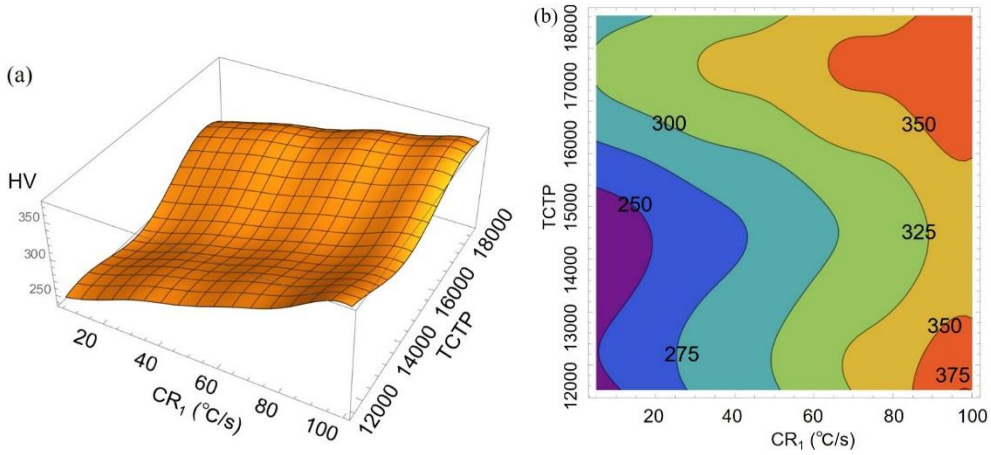

Fig. 15 Hardness prediction subsystem for WM after 1-cycle+tempering (with constant T_{p1} = 1350 °C):

(a) 3D figure, and (b) 2D contour figure.

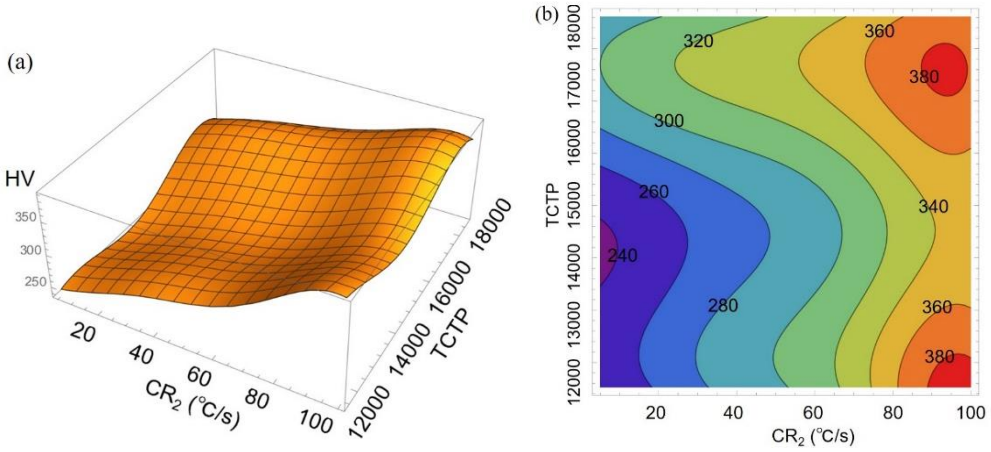

Fig. 16 Hardness prediction subsystem of WM after 2-cycle+tempering (with constant T_{p1} = 1350 °C, CR_1 = 90 °C/s, T_{p2} = 1200 °C):

(a) 3D figure, and (b) 2D contour figure.

4.3 Effectiveness of the developed hardness prediction subsystem for WM

The effectiveness of the developed hardness prediction subsystem for the WM (MG-S56X) was verified by comparing the hardness results for the raw WM exposed to arbitrary thermal cycles under the conditions listed in Table V. Forty arbitrary thermal cycles were selected that contained 10 conditions for each type of thermal cycle.

The measured hardness of the WM (MG-S56X) subjected to arbitrary thermal cycles was compared with the results calculated by the previously developed hardness prediction subsystem for the WM, and the correlation coefficients between the measured and calculated results are summarized in Fig.

17. There was good agreement between the calculated hardness and measured result, with correlation coefficients for the four types of thermal cycles that were greater than 0.83. This indicated that the hardness of the raw WM (MG-S56X) subjected to any combination of thermal cycles that could be generated during multi-pass welding could be predicted using the newly developed hardness prediction subsystem for the WM if the thermal cycle parameters are known.

Table V Thermal cycle parameters for four types of arbitrary thermal cycles

Parameters	T_{p1} (℃)	CR_1 (℃/s)	T_{p2} (℃)	CR_2 (℃/s)	T_{te} (℃)	t_h (s)	Mea. HV	Cal. HV
1-cycle	1300	WQ					383.2	374.4
	1300	60					300.2	309.6
	1300	10					242.0	239.0
	1100	WQ					399.6	370.3
	1100	60					269.8	303.9
	1100	10					251.0	244.4
	1000	WQ					402.8	386.9
	1000	10					257.2	263.7
	500	60					290.6	289.9
	500	10					284.0	279.6
2-cycle	1200	WQ	1000	60			270.0	303.6
	1200	60	950	10			248.0	241.3
	1200	10	700	WQ			271.2	313.7
	1100	WQ	750	60			345.2	324.0
	1100	60	950	10			241.0	241.2
	1100	10	1200	WQ			366.0	372.4
	950	WQ	1200	60			280.6	304.0
	950	10	800	10			253.8	256.5
	800	60	1200	WQ			386.0	360.4
	800	10	950	60			276.2	302.9
1-cycle +tempering	1250	WQ			680	120	354.8	353.4
	1250	60			600	10	287.6	293.0
	1250	10			680	660	282.2	267.0
	950	WQ			550	60	343.4	315.6
	950	60			450	30	280.4	275.2
	950	10			450	10	265.4	261.1
	850	WQ			680	10	340.4	337.2
	850	10			600	30	271.4	274.9
	750	60			450	10	333.0	289.9
	750	10			550	30	332.4	284.8
2-cycle +tempering	1300	WQ	1150	60	680	660	294.0	317.2
	1300	60	850	10	600	120	264.6	278.4
	1300	10	750	WQ	550	10	268.4	291.3
	1150	WQ	750	WQ	660	660	342.6	333.0
	1150	60	1150	10	600	60	257.6	262.5
	1150	10	850	60	450	20	260.2	267.8
	850	WQ	1000	WQ	550	20	351.0	344.0
	850	10	750	60	450	10	270.2	267.2
	750	60	1150	10	680	120	282.6	292.9
	750	10	850	60	550	10	273.4	268.6

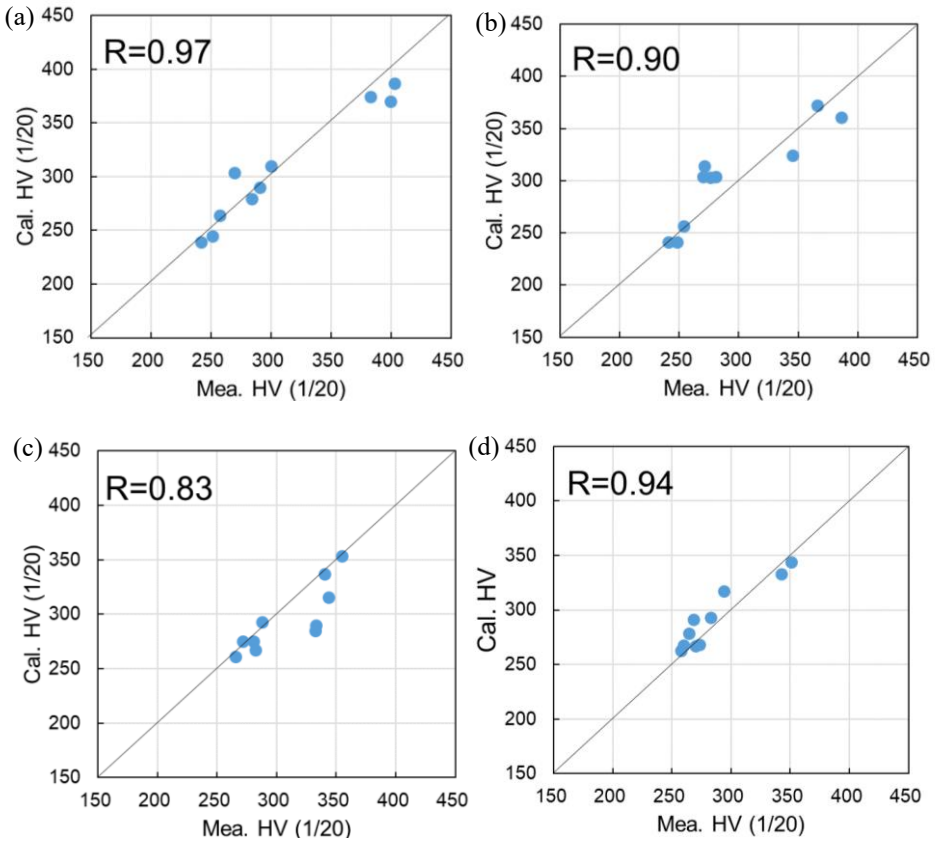

Fig. 17 Comparison of measured hardness and calculated result for WM (MG-S56X) after four types of arbitrary thermal cycles:
(a) 1-cycle, (b) 2-cycle, (c) 1-cycle+tempering, and (d) 2-cycle+tempering.

5. Hardness prediction system for entire weld, including both WM and HAZ of multi-pass weld

To quickly determine the effectiveness of multi-pass welding conditions, a hardness prediction system for the entire multi-pass weld, including both the WM and HAZ, was developed by combining the NN-based hardness prediction system for the WM of a multi-pass weld developed in this study and the previously proposed hardness prediction system for the HAZ [8]. The effectiveness of the newly developed hardness prediction system for the entire multi-pass weld was validated by comparing the predicted hardness with the measured result.

5.1 Construction of hardness prediction system for multi-pass welds

Fig. 18 shows a flowchart of the hardness prediction system for an entire multi-pass weld, including both the WM and HAZ, which includes the following subsystems. First, an FEM simulation was performed to analyze the thermal cycles in both the WM and HAZ parts. Second, the WM, HAZ and base metal (BM) parts could be classified according to the maximum temperature of the FEM-

simulated thermal cycles. Based on the simulated thermal cycles, the grid node where the maximum temperature was lower than 400 °C was treated as the BM. When the maximum temperature was higher than 1500 °C, the grid node was categorized as the WM, and the hardness was calculated using the hardness prediction subsystem for the WM (MG-S56X) developed in this study. All the other grid nodes with at least one maximum temperature in the range of 400-1500 °C were considered to be part of the HAZ, and the hardness was calculated using the previously constructed hardness prediction subsystem for A533B steel [8]. Then, based on the predicted hardness for every grid node of the whole weld, including both the WM and HAZ, the visual hardness distribution of the multi-pass weld could be illustrated by color mapping. Finally, the effectiveness of the proposed hardness prediction system of an entire multi-pass weld, including both the WM and HAZ, was verified by comparing the predicted hardness with the measured result.

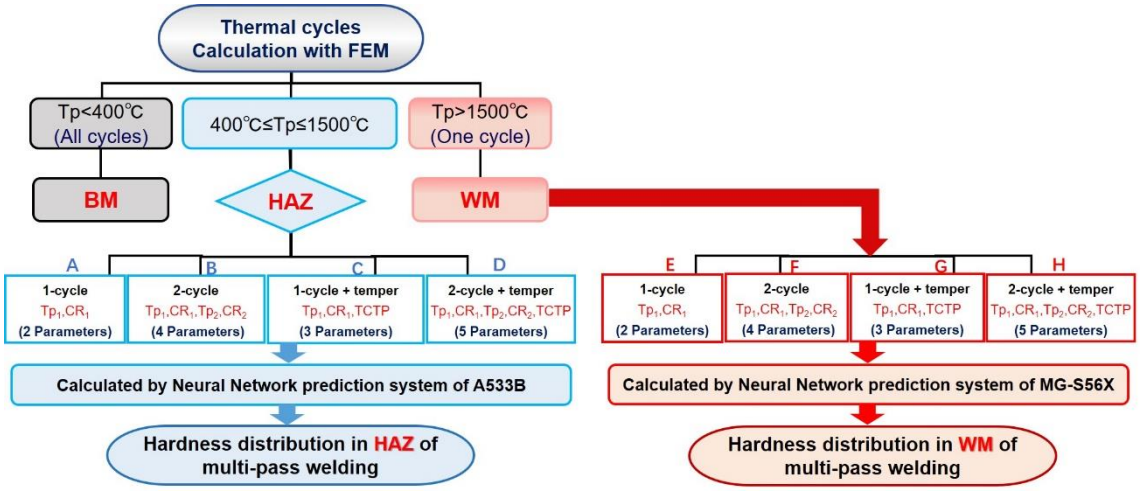

Fig. 18 Flow chart of hardness prediction for entire weld, including both the WM and HAZ of multi-pass weld.

5.2 FEM simulation of thermal cycles during multi-pass welding

In this study, 19-pass welding was used to verify the effectiveness of the proposed hardness prediction system for multi-pass welds. The thermal cycles in multi-pass welds were simulated using the thermal elastic plastic FEM software JWRIAN, which was specifically developed for predicting the thermal history, residual stress, and deformation of a weld [13]. Fig. 19 shows the mesh model created by PATRAN and the built-up sequence of welds after 19 passes based on the actual cross-section of the welded sample. The mesh in the WM and HAZ was finer than that in the BM. In addition, the red dotted lines were far from the sample surface with different distances of z = -1.0 and -8.5 mm.

Fig. 20 shows the simulated peak temperature distribution in the middle cross-section after 19-pass welding. The part where the peak temperature was higher than 1500 °C was considered the WM, and

the part where the peak temperature was in the range of 400-1500 °C was treated as the HAZ.

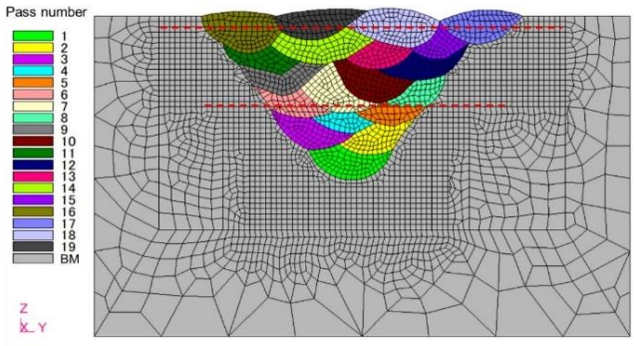

Fig. 19 Cross-section of mesh model and built-sequence after 19-pass welding for FEM analysis.

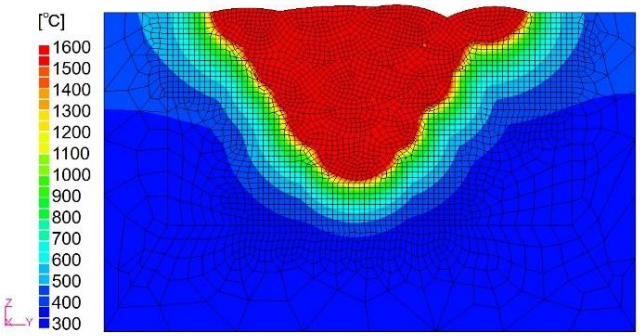

Fig. 20 Simulated peak temperature distribution after 19-pass welding.

5.3 Predicted hardness distribution in multi-pass weld

Based on the simulated thermal history of each grid node, the hardness values for both the WM and HAZ were calculated using the method explained in section 5.1. Fig. 21 presents the predicted hardness distribution in both the WM and HAZ as a color chart map, with the dotted curves representing the edge of each weld pass. The hardness values in both the WM and HAZ are displayed in rainbow colors for different hardness levels. The predicted hardness results showed that a hardness above 350 HV (industry-required specification) appeared only in the coarse grain zone of the HAZ of the final welding layer. It is also found that the hardness in the entire WM area was lower than 350 HV after the 19-pass welding. A hardness of 350 HV is the required specification for low-alloy steel in the industry. A weld with a hardness higher than 350 HV is considered to be prone to defects. Therefore, the welding parameters must be modified if the predicted hardness exceeds 350 HV.

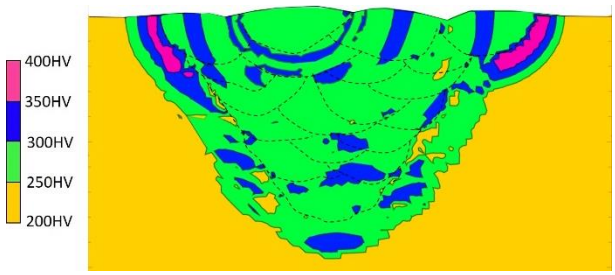

Fig. 21 Predicted hardness distribution after 19-pass welding.

5.4 Validity of the developed hardness prediction system for multi-pass weld

To verify the effectiveness of the proposed hardness prediction system for an entire multi-pass weld, including both the WM and HAZ, the hardness of a 19-pass weld was experimentally measured, as visually shown in Fig. 22(a). Compared with the predicted hardness distribution shown in Fig. 22(b), it can be found that the predicted hardness distribution is in good agreement with the measured result. In addition, it was confirmed that the hardened zone with a hardness above 350 HV only appeared in the coarse grain zone of the HAZ of the final welding layer in both the measured and predicted results. The hardness of the entire WM area was also found to be less than 350 HV.

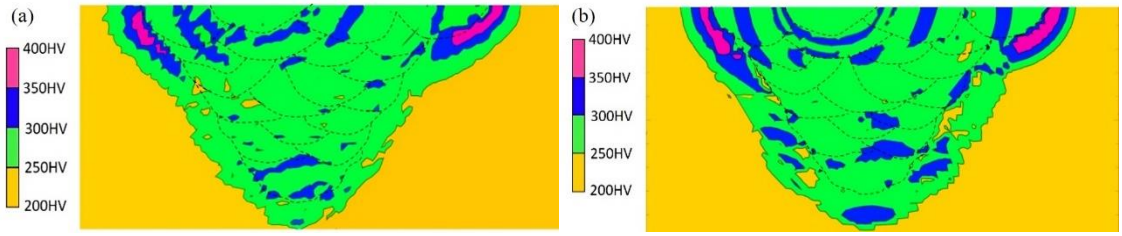

Fig. 22 Comparison of measured and predicted hardness distributions after 19-pass welding: (a) measured hardness distribution, and (b) predicted hardness distribution.

In addition, a one-dimensional hardness comparison between the predicted and the measured values was performed along the red dotted lines shown in Fig. 19 at different distances from the sample surface (z = -1.0 and -8.5 mm) in the welded cross-section. Fig. 23 shows the hardness comparison results for the two measured lines, and the correlation relationship between the measured hardness and predicted result is summarized in Fig. 24. It was found that the predicted hardness values corresponded well with the measured values, with high correlation coefficients along the two lines of 0.88 and 0.87.

From the results of the two-dimensional hardness color mapping comparison and one-dimensional line comparison, it was found that the newly developed hardness prediction system for an entire weld, including both the WM and HAZ of a multi-pass weld, was very useful and effective. In summary, the hardness of an entire multi-pass weld could be predicted before performing the actual multi-pass welding using the above method. This would allow the appropriate welding conditions to be selected

prior to the actual multi-pass welding, which would be very useful for the multi-pass welding in the industry.

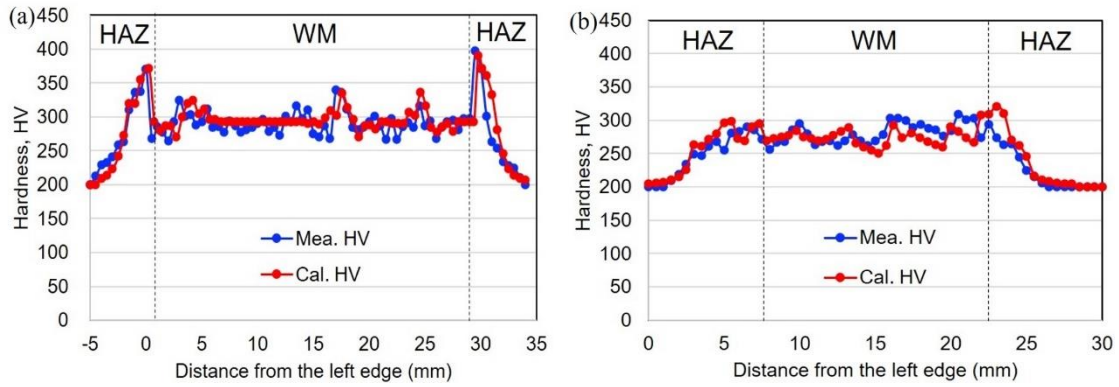

Fig. 23 Comparison of calculated and measured hardness distributions at the two lines after 19-pass welding:

(a) z = -1.0 mm, and (b) z = -8.5 mm.

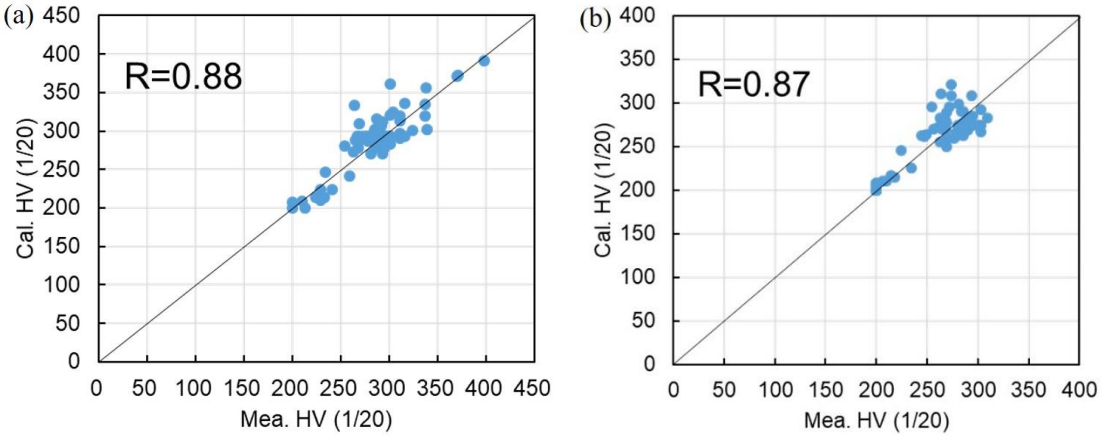

Fig. 24 Relationship between calculated and measured hardness values at two lines after 19-pass welding:

(a) z = -1.0 mm, and (b) z = -8.5 mm.

6. Conclusions

A NN-based hardness prediction system for the WM of a multi-pass weld was developed in this study, which allowed the development of a hardness prediction system for an entire multi-pass weld, including both the WM and HAZ, by combining the previously constructed hardness prediction system for the HAZ with this new system. The following conclusions were drawn.

(1) Based on a hardness database obtained experimentally, a new hardness prediction system for the

WM of a multi-pass weld was developed using the RBF-NN.

(2) In combination with the previously proposed hardness prediction system for the HAZ, a new hardness prediction system for an entire multi-pass weld, including both the WM and HAZ, was developed.

(3) The hardness values in both the WM and HAZ after 19-pass welding were predicted using the newly proposed prediction system for the entire multi-pass weld, based on the FEM-simulated thermal cycle parameters.

(4) It was found that the predicted hardness values were in good agreement with the experimentally measured results, which indicated that the newly proposed hardness prediction system for the entire multi-pass weld, including both the WM and HAZ, would be effective for selecting appropriate welding conditions prior to actual multi-pass welding.

Acknowledgment

The authors would like to gratefully acknowledge the assistance of Mr. Akihiro Mukai, Master of the Graduate School of Engineering, Osaka University, Japan.

Conflict of Interest Statement

On behalf of all authors, the corresponding author states that there is no conflict of interest.

References

1. S. Ganguly, J. Sule, and M.Y. Yakubu: *Journal of Materials Engineering and Performance*, 2016, vol. 25, pp. 3238-3244.
2. M.A. Valiente Bermejo, K. Hurtig, D. Eyzop, and L. Karlsson: *Applied Sciences*, 2019, vol. 1050, pp. 1-18.
3. J.L. Caron and J.W. Sowards: *Comprehensive Materials Processing*, 2014, vol. 6, pp. 151-179.
4. M.T. Abdullah, M.L.N. Ajian, and P.E. Sarah: *Journal of Mechanical Engineering Research and Developments (JMERD)*, 2019, vol. 42, pp. 202-204.
5. A. Mashhuriazar, H. Omidvar, Z. Sajuri, C.H. Gur, and A.H. Baghdadi: *Metals,* 2020, vol. 10, 1453-1469.
6. L. Yu, Y. Nakabayashi, M. SaSa, S. Itoh, M. Kameyama, S. Hirano, N. Chigusa, K. Saida, M. Mochizuki, and K. Nishimoto: *ISIJ International*, 2011, vol. 51, pp. 1506-1515.
7. L. Yu, K. Saida, M. Mochizuki, M. Kameyama, N. Chigusa, and K. Nishimoto: *E-Journal of Advanced Maintenance*, 2014, vol. 6, pp. 34-47.
8. L. Yu, K. Saida, S. Hirano, N. Chigusa, M. Mochizuki, and K. Nishimoto: *Welding in the World*, 2017, vol. 61, pp. 483-498.
9. J. Feng, W. Guo, N. Irvine1, and L. Li: *The International Journal of Advanced Manufacturing*

Technology, 2017, vol. 88, pp. 1821-1830.

10. D. Dittrich, R. Schedewy, B. Brenner, and J. Standfuß: *Physics Procedia*, 2013, vol. 41, pp. 225-233.
11. K. Ueda, S. Yamashita, A. Takada, N. Sahara, T. Ogura, and K. Saida: *Welding International*, 2020, vol. 34, pp. 388-398.
12. R. Viswanathan, D.W. Gandy, and S.J. Findlan: *EPRI*, Palo Alto, CA: 1998. TR-111757.
13. D. Deng, H. Murakawa, and M. Shibahara: *Computational Materials Science*, 2010, vol. 48, pp. 187-194.
14. N. Yanagida and K. Saito: *Mechanical Engineering Journal*, 2016, vol. 3, pp. 1-12.
15. Z. Wang, H. Zhang, C. Guo, W. Liu, Z. Yang, X. Sun, Z. Zhang, and F. Jiang: *Journal of Materials Science*, 2016, vol. 51, pp. 4996-5007.
16. E.J. Pavlina, J.G. Speer, and C.J.V. Tyne: *Scripta Materialia*, 2012, vol. 66, pp. 243-246.
17. Y. Ohmori: *Transactions ISIJ*, 1972, Vol. 12, pp. 350-357.
18. Y. Tanaka, F. Pahlevani, S.C. Moon, R. Dippenaar, and V. Sahajwalla: *Scientific Reports*, 2019, vol. 9, pp. 1-12.
19. Y. Ueshima, Y. Sawada, S. Mizoguchi, and H. Kajioka: *Metallurgical Transactions A*, 1989, vol. 20A, pp. 1375-1383.
20. D.C. Saha, S.S. Nayak, E. Biro, A.P. Gerlich, and Y. Zhou: *Metallurgical and Materials Transactions A*, 2014, vol. 45A, pp. 6153-6162.
21. Y. Zhang, C. Zhao, M. Sato, G. Miyamoto, and T. Furuhara: *ISIJ International*, 2021, vol. 61, pp. 1641-1649.
22. V.D. Manvatkar, A. Arora, A. De, and T. DebRoy: *Science and Technology of Welding & Joining*, 2012, vol. 17, pp. 460-466.
23. E.A. Metzbower, D.L. Olson, and N. Yurioka: *Science and Technology of Welding & Joining*, 2009, vol. 14, pp. 566-569.
24. D. Casasent and X. Chen: *Neural Networks*, 2003, vol. 16, pp. 529-535.